

Large-eddy simulation of turbulent channel flow at transcritical states

A. Doehring^{*}, T. Kaller, S.J. Schmidt, N.A. Adams

Institute of Aerodynamics and Fluid Mechanics, Department of Mechanical Engineering, Technical University of Munich, Boltzmannstr. 15, 85748 Garching, Germany

ARTICLE INFO

Keywords:

LES
Transcritical
Channel flow
Turbulent Prandtl number

ABSTRACT

We present well-resolved large-eddy simulations (LES) of a channel flow solving the fully compressible Navier–Stokes equations in conservative form. An adaptive look-up table method is used for thermodynamic and transport properties. A physically consistent subgrid-scale turbulence model is incorporated, that is based on the Adaptive Local Deconvolution Method (ALDM) for implicit LES. The wall temperatures are set to enclose the pseudo-boiling temperature at a supercritical pressure, leading to strong property variations within the channel geometry. The hot wall at the top and the cold wall at the bottom produce asymmetric mean velocity and temperature profiles which result in different momentum and thermal boundary layer thicknesses. Different turbulent Prandtl number formulations and their components are discussed in context of strong property variations.

1. Introduction

Supercritical fluids, whose pressure and temperature are above their critical values, are used in many engineering applications, as for example in gas turbines, supercritical water-cooled reactors (SCWRs) and liquid rocket engines (LRE). They are characterized by a gas-like diffusivity, a liquid-like density and their surface tension is approaching zero. The latter can be observed in the experimental study with cryogenic jets of Mayer and Tamura (1996). At a supercritical pressure the fluid in the experiments was forming finger-like entities with a continuous phase transition instead of droplets and ligaments. Studies, for instance Simeoni et al. (2010), disagree with a continuous phase transition, but have shown a supercritical liquid-like (LL) and gas-like (GL) region with a pseudo-boiling line (PBL), which extends the classical liquid–vapor-coexistence line. In this regard, the transcritical condition refers to the temperature variation from compressed fluid ($T < T_{cr}$, $p > p_{cr}$) to supercritical state ($T > T_{cr}$, $p > p_{cr}$). Furthermore, strong non-linear property variations are present in the vicinity of the PBL, which are induced by intermolecular repulsive forces. As a consequence, the heat transfer and shear forces in wall bounded flows are affected significantly, leading to poor prediction capabilities of Reynolds-averaged Navier–Stokes simulations (RANS) including established turbulence models (Yoo, 2013). Thus, effects like the heat transfer enhancement as well as the onset of heat transfer deterioration in transcritical and supercritical flows cannot be captured correctly. For this reason, high fidelity data are required to assess the heat transfer

prediction capabilities of numerically less expensive turbulence models.

Ma et al. (2018) has performed a Direct numerical simulation (DNS) of a transcritical channel flow using an entropy-stable double-flux model in order to avoid spurious pressure oscillations. They have observed the presence of a logarithmic scaling of the structure function and a k^{-1} scaling of the energy spectra, which supports the attached-eddy hypothesis in transcritical flows. A heated transcritical turbulent boundary layer over a flat plate has been investigated by Kawai (2019) with DNS. His study shows large density fluctuations which are induced by strong changes of thermodynamic properties in the vicinity of the pseudo-boiling. Furthermore, these fluctuations evoke non-negligible Favre-averaged velocity fluctuations which are associated with a turbulent mass flux. In addition, velocity transformations such as the van Driest transformation, the semi-local scaling by Huang et al. (1995) and the transformation by Trettel and Larsson (2016) have failed in transcritical boundary layers. This has also been ascertained by Ma et al. (2018) and Doehring et al. (2018).

In this study, we conduct well-resolved large-eddy simulations (LES) of a transcritical channel flow. The wall temperatures are set in order to enclose pseudo-boiling. Two cases with a different bulk pressure are performed to vary the intensity of non-linear effects. This setup is distinguished by a pseudo-boiling position at $y^+ \approx 14$ and $y^+ \approx 24$ close to the cold wall, whereby the influence of strong property variations on turbulent boundary layers but especially on turbulent eddy viscosity and thermal diffusivity are studied.

^{*} Corresponding author.

E-mail address: alex.doehring@tum.de (A. Doehring).

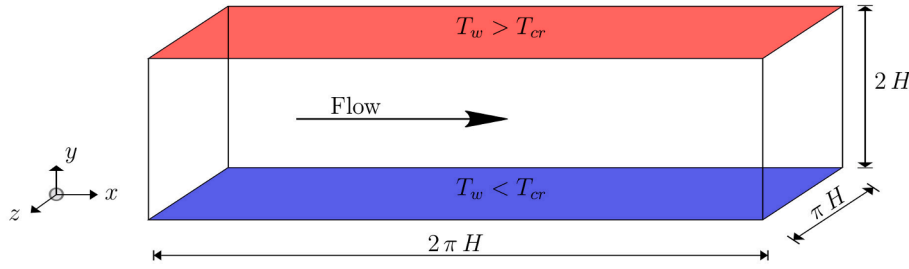


Fig. 1. Computational domain with a hot wall above and a cold wall below the critical temperature at supercritical pressure.

2. Numerical model

LES are performed solving the three-dimensional compressible continuity, momentum and total energy equations. A finite-volume method is applied in order to spatially discretize the governing equations on a block structured, curvilinear grid. An explicit second-order low-storage four-stage Runge–Kutta method with enhanced stability region is applied for time advancement (Schmidt et al., 2006). The compact four cell stencil approach by Egerer et al. (2016) is used to compute the convective fluxes. A discontinuity detecting sensor functional is used to switch the flux calculation between a linear fourth-order reconstruction for high accuracy and a more stable upwind-biased scheme. A physically consistent subgrid-scale turbulence model based on the Adaptive Local Deconvolution Method (ALDM) (Hickel et al., 2006, 2014) is included in the convective flux calculation. Viscous fluxes are determined by a linear second-order centered scheme. An extensive study of the ALDM subgrid-scale model in the context of trans- and supercritical flows was performed by Matheis and Hickel (2018).

Thermodynamic and transport properties are obtained using an adaptive look-up table method based on the REFPROP database (Lemmon et al., 2013). One table is generated for the fluid domain imposing density and internal energy constraints and a second table is used for the boundary conditions imposing pressure and temperature constraints. Thermodynamic and transport properties are extracted from the tabulated look-up database via trilinear interpolation.

3. Setup

A generic channel flow configuration is used to focus this study on transcritical heat transfer and on the impact of non-linear thermodynamic effects on turbulent flows. Periodic boundary conditions are imposed in stream- and spanwise directions, and isothermal no slip boundary conditions are applied at the top and bottom walls. The channel geometry is depicted in Fig. 1. The dimensions are based on the channel half-height H with a size of $2\pi H \times 2H \times \pi H$ in the streamwise, wall-normal and spanwise direction, respectively. In order to fulfill the resolution requirements at walls, we use a hyperbolic stretching law in wall-normal direction, whereas a uniform grid spacing is used in stream- and spanwise directions. The grid parameters are summarized in Table 1 including the number of grid points in each direction N_x , N_y , N_z and the resolution with respect to wall units $\Delta x^+ = \Delta x \rho_w u_\tau / \mu_w$, with the friction velocity $u_\tau^2 = (\tau_w / \rho_w)$ and the wall shear stress $\tau_w = (\mu \partial u / \partial y)|_w$.

Note, that the resolution is based on the whole cell size, but the flow variables are evaluated at the cell center. Therefore, the effective minimum wall distance is $\Delta y_{\min}^+ / 2$. In order to estimate the mesh resolution in terms of thermal scales we employ the ratio between the Batchelor scales η_B and the Kolmogorov scales η introduced by Monin and Yaglom (1975)

$$\frac{\eta_B}{\eta} = \left(\frac{1}{Pr} \right)^{1/2}. \quad (1)$$

This ratio has been used in context of heated transcritical and ideal gas boundary layers by Zonta et al. (2012), Lee et al. (2013), Ma et al.

Table 1
Summary of grid parameters.

	TCF47	TCF57
$N_x \times N_y \times N_z$	192 × 192 × 192	192 × 192 × 192
$L_x \times L_y \times L_z$	$2\pi H \times 2H \times \pi H$	$2\pi H \times 2H \times \pi H$
$\Delta x_{\text{cold}}^+ \times \Delta x_{\text{hot}}^+$	23.1 × 9.5	24.3 × 11.1
$\Delta z_{\text{cold}}^+ \times \Delta z_{\text{hot}}^+$	11.5 × 4.8	12.2 × 5.6
$\Delta y_{\min, \text{cold}}^+ \times \Delta y_{\min, \text{hot}}^+$	0.77 × 0.32	0.82 × 0.37
$\Delta y_{\max, \text{cold}}^+ \times \Delta y_{\max, \text{hot}}^+$	16.8 × 6.9	17.7 × 8.1
$\Delta y_{T, \min, \text{cold}}^+ \times \Delta y_{T, \min, \text{hot}}^+$	1.12 × 0.27	1.14 × 0.32
$\Delta y_{T, \max, \text{cold}}^+ \times \Delta y_{T, \max, \text{hot}}^+$	21.3 × 8.7	24.47 × 11.12

(2018), Kaller et al. (2019) and Kawai (2019). We adapt this relationship for the LES context by assuming a proportionality between the thermal and viscous scales including the molecular Prandtl number

$$l_T^+ = l^+ / \sqrt{Pr}, \quad (2)$$

$$\Delta y_T^+ = \Delta y / l_T^+ = \Delta y^+ \sqrt{Pr}. \quad (3)$$

The error made with the used assumption reduces with an increased grid resolution approaching the ratio of Eq. 1. Ma et al. (2018) reported that the grid resolution is governed by the thermal scales and not the viscous scales due to a varying molecular Prandtl number. Since the molecular Prandtl number is partly greater than one in our LES implies that the thermal scales are also smaller than the viscous scales. This can be observed in Table 1 and Fig. 2 by means of dimensionless grid resolution of Eq. 3. The thermal scales are relevant at the cold wall and the

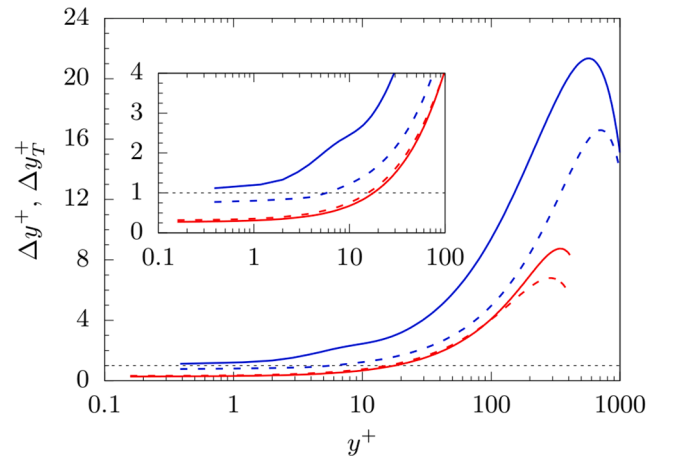


Fig. 2. Wall-normal cell sizes based on the viscous length scale l^+ ---- and thermal length scale $l_T^+ = l^+ (\overline{Pr})^{-0.5}$ ——— for case TCF47 over the dimensionless wall distance y^+ . The cold wall resolution is shown in blue and the hot wall resolution in red. A zoomed in figure is included showing the vicinity of the wall. The thin dashed black line indicates $\Delta y^+ = 1$ and $\Delta y_T^+ = 1$, respectively.

viscous scales at the hot wall regarding the resolution requirements. Based on Eq. 3 the thermal scales are slightly under-resolved, see Table 1. However, the linear behavior of the temperature profile in the viscous sublayer towards the wall shown in Fig. C.17 in the appendix implies a sufficient resolution.

In addition to the minimum and maximum resolution values a grid sensitivity study has been performed due to the strong property variations, see Appendix C. The refinement of the grid leads to an adjustment of the wall shear stress and wall heat flux, thus, to a bulk pressure, which varies from one level to another. As a consequence, the bulk density has been adjusted by trial and error due to non-linearity of the thermodynamics in order to match the bulk pressure for all grid levels. As a trade-off between accuracy and computational cost the resolution of 192^3 has been chosen, although the Reynolds stresses in the streamwise direction do not show a fully converged solution.

The same grid has been used for all performed LES simulations. Roughness and gravity effects are not considered in the simulations in order to ascribe the observed results to non-linear thermodynamic effects and not an interaction of multiple influences. The subscript w refers to values at the wall, b to bulk parameters, cr to critical values, pb to values obtained at the pseudo-boiling position, c to values at the cold wall and h to values at the hot wall.

Methane is used as working fluid with its critical pressure of $p_{cr} = 4.5992$ MPa at a critical temperature of $T_{cr} = 190.564$ K. Two simulations have been performed by adjusting the bulk density in order to obtain the desired bulk pressure. This method is similar to Kim et al. (2019). The intention is to create two cases with certain distance to the critical point in order to capture different intensities of non-linear thermodynamic effects. The naming convention for the performed simulations is related to the obtained bulk pressure. Simulation TCF47 features a bulk pressure of $p_b = 4.75$ MPa, thus a reduced pressure of $p_r = p_b/p_{cr} = 1.03$, whereas simulation TCF57 uses a bulk pressure of $p_b = 5.70$ MPa and a reduced pressure of $p_r = p_b/p_{cr} = 1.24$. In both simulations the cold wall temperature is set to $T_{wc} = 180$ K ($T_{wc} < T_{cr}$) and the hot wall temperature is $T_{wh} = 400$ K ($T_{wh} > T_{cr}$), thus a temperature ratio of $T_{wh}/T_{wc} = 2.22$ is obtained. These boundary conditions encompass the pseudo-boiling temperature and result in a density ratio of $\rho_{wc}/\rho_{wh} = 12.8$.

A body force in the momentum and energy equation is added to maintain a constant mass flux. As a result, a bulk velocity of $u_b = 74$ ms^{-1} and a maximum Mach number of 0.27 are reached. The additional body force is based on Brun et al. (2008). Several flow parameters for TCF47 and TCF57 are summarized in Table 2.

4. Results

In the following, the mean flow properties are analyzed by averaging in time and subsequently in streamwise and spanwise direction after reaching a quasi-stationary state. The Favre average is defined as $\bar{\phi} = \overline{\rho\phi}/\bar{\rho}$ and the Reynolds average is an ensemble average denoted with an overline $\bar{\phi}$. The fluctuations are represented as double prime ϕ'' or single prime ϕ' with respect to Favre and Reynolds averages, respectively. For both simulations over 100 flow-through-times have been used for the computation of the mean values. This high number is necessary since

Table 2
Summary of flow parameters.

	TCF47	TCF57
ρ_b [kg/m^3]	74.12	92.60
p_b [MPa]	4.75	5.70
T_b [K]	215.5	219.2
q_{wc}, q_{wh} [MW/m^2]	4.45, 4.2	5.50, 5.2
$Re_{\tau_c}, Re_{\tau_h} = u_{\tau}H/\nu$	705, 290	745, 338
$Re_b = u_bH/\nu$	16500	18500

changes close to the wall are developing very slowly, especially for high order statistics, as for instance triple correlations. For further information about averaging techniques in the context of strongly correlated fluid variables we refer to Huang et al. (1995) and Smits and Dussauge (2006).

4.1. Mean flow field

The Favre averaged mean velocity and temperature profiles are shown in Fig. 3(a) and (b). The temperature is scaled using the wall temperatures $\theta_T = (T - T_{wc})/(T_{wh} - T_{wc})$ and the velocity is scaled by the bulk value u_b . The velocity peak is shifted towards the hot wall, due to the one-sided heating from the top and the associated thermal expansion. As a consequence, the momentum boundary layer at the cold wall is thicker than at the hot wall $\delta_{M_c} > \delta_{M_h}$. The boundary layer thicknesses are determined by using the locus of zero total shear stress $\tau_{tot} = 0$. Except for a minor flattening of the peak value in TCF57 compared to TCF47 no significant difference can be observed between the two velocity profiles. The temperature distribution features strong gradients in the vicinity of the walls. In the vicinity of the cold wall the temperature profile is flattened due to the specific heat capacity peak in Fig. 3(d). The increase of the bulk density in TCF57 also leads to a slight increase of the bulk temperature, which is mostly visible at $y/H < 0.0$. The thermal boundary layers are defined as the distance between the wall and the locus of minimum heat transfer $\bar{q} = -\overline{\lambda\partial T/\partial y}$. Thus, the thermal boundary layer thickness at the hot wall is approximately 5.5 times the thermal boundary layer thickness at the cold wall. Fig. 3(c) and (d) show the mean density $\theta_\rho = (\rho - \rho_{wh})/(\rho_{wc} - \rho_{wh})$ and specific heat capacity distributions. The adjustment of the bulk density in order to obtain a higher bulk pressure can be observed by an elevated profile for TCF57. The higher bulk pressure with increased distance to the critical pressure of methane leads to a smaller specific heat capacity peak. The pseudo-boiling positions are determined by means of the c_p peak with

$$y_{pb47}/H \approx -0.980 \rightarrow y^+ \approx 14 \quad (4)$$

$$y_{pb57}/H \approx -0.969 \rightarrow y^+ \approx 23. \quad (5)$$

Due to strong property variations the mean Prandtl number $\bar{Pr} = \overline{\mu c_p}/\bar{\lambda}$ varies over the channel height from 0.76 to 5.2, see Fig. 3(e). Especially close to the pseudo-boiling position strong changes are observed, where momentum diffusivity is dominating and thermal diffusivity $\bar{\alpha} = \overline{\lambda}/(\overline{\rho c_p})$ reaches a minimum, see Fig. 3(f). This stems from the specific heat capacity peak acting as a heat sink and leading to the observed flattening of the temperature profile. In addition, a local Prandtl number minimum occurs after the peak value for TCF47 shown in the inset of Fig. 3(f). This local minimum is not observed for TCF57 or in DNS studies (Kim et al., 2019; Ma et al., 2018; Kawai, 2019) and stems from the thermal diffusivity showing a local maximum. We attribute this to real gas effects, since the bulk pressure is very close to the critical value of methane.

4.2. Turbulent Prandtl number

The highly variable Prandtl number of super- and transcritical channel flows affects the thermal boundary layer and the heat transfer over the walls. Thus, RANS turbulence models, which do not account for a highly variable Prandtl number, fail in predicting the correct heat transfer (Yoo, 2013). Likewise the turbulent Prandtl number Pr_t may lead to wrong heat transfer predictions in RANS. It is used as a modeling parameter to close RANS equations by providing a relationship between the turbulent eddy thermal diffusivity ϵ_H and turbulent eddy viscosity ϵ_M . In most cases Pr_t is set to a constant value which is based upon the strong Reynolds analogy (SRA), assuming a correlation between the turbulent heat transfer and the turbulent momentum transfer resulting in

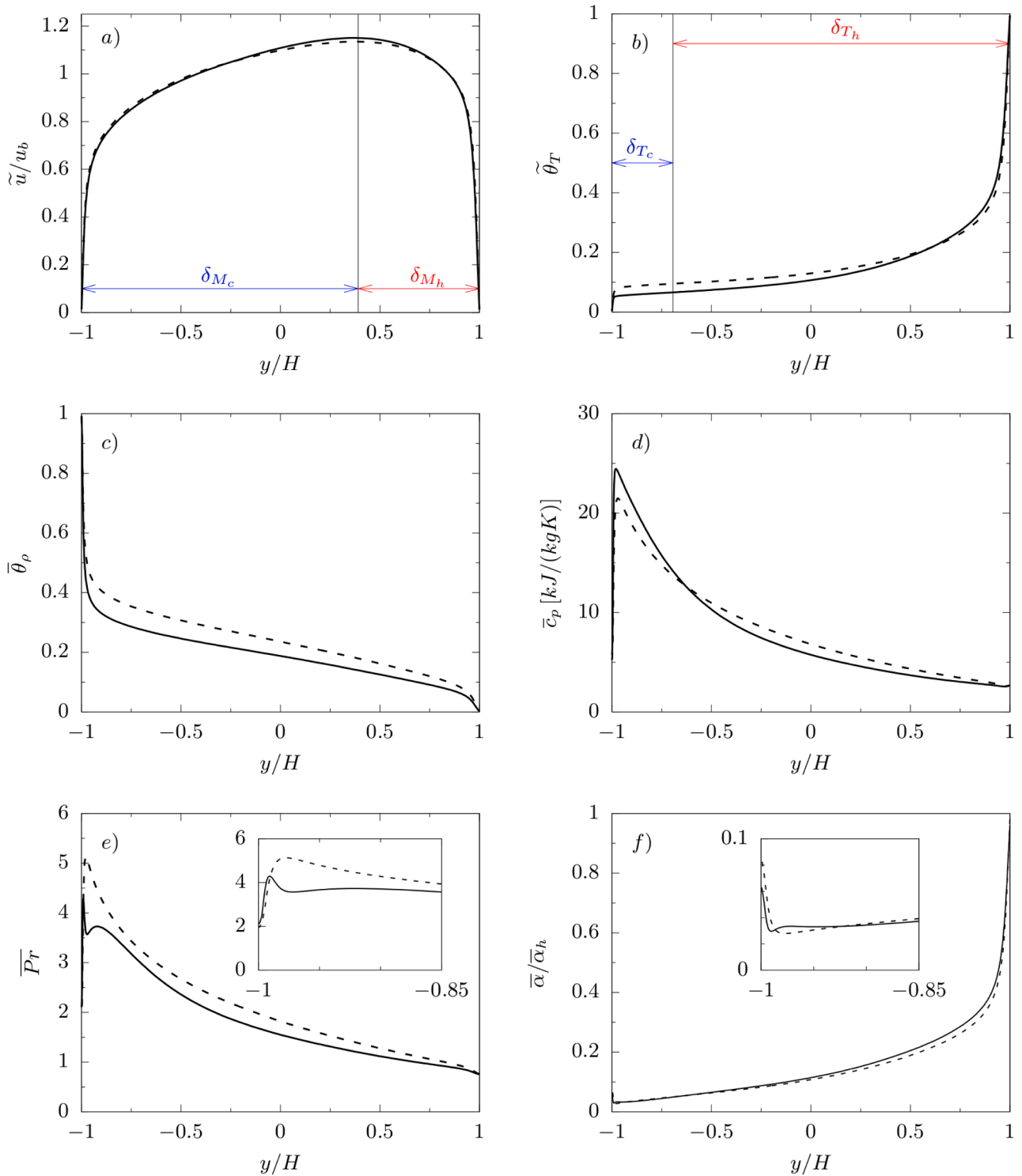


Fig. 3. Mean profiles are depicted over the channel height for case TCF47 — and TCF57 - - -. Favre averaged mean velocity and temperature are shown in a) and b) and mean density and specific heat capacity in c) and d), respectively. Momentum δ_M and thermal δ_T boundary layer thicknesses are included for the cold and hot side regarding case TCF47. Mean Prandtl number e) and mean thermal diffusivity f) profiles are shown over the channel height. The mean thermal diffusivity is scaled with the value at the hot wall $\bar{\alpha}_h$. A zoomed in figure is included for the area close the cold wall.

$$Pr_t = \frac{\epsilon_M}{\epsilon_H} = 1. \tag{6}$$

Experimental and DNS studies have shown, that this simple assumption is not correct, since the turbulent Prandtl number is at least dependent on the wall distance and the molecular Prandtl number, $Pr_t = f(y^+, Pr)$ (Kays, 1994). It was observed, that Pr_t is relatively constant in

the logarithmic region, whereas it is increasing towards the wall and decreasing in the wake region.

For the analysis of the turbulent Prandtl number in the transcritical LES we included two different formulations taken from the literature:

Incompressible:

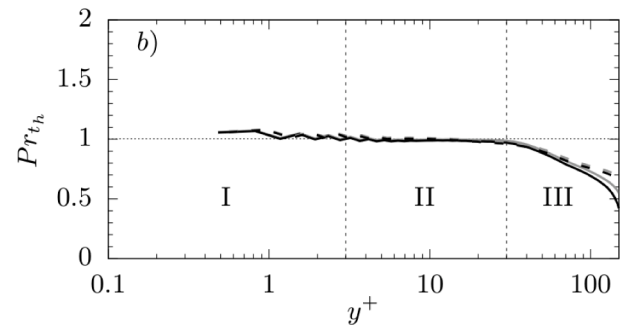
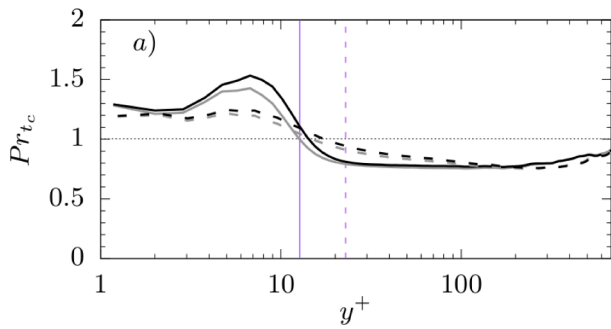


Fig. 4. Turbulent Prandtl number at the cold wall (a) and the hot wall (b) over wall units y^+ for case TCF47 — and TCF57 ---. Included are the incompressible (grey) and compressible (black) formulation. The pseudo boiling position at the cold wall is indicated by a vertical purple line.

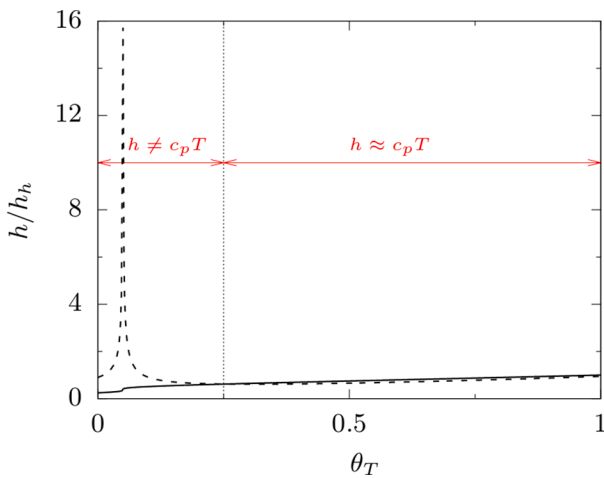


Fig. 5. Comparison of enthalpy h — with the relationship for a calorically perfect gas $c_p T$ --- at a bulk pressure of $p_b = 47\text{bar}$. Enthalpy h , specific heat capacity c_p and temperature T are taken from the NIST data base. The profiles are scaled with the hot wall value and presented over the scaled temperature range which is present within the channel.

$$Pr_t = \frac{\overline{u'v'}}{\overline{v'T'}} \frac{\partial \overline{T}/\partial y}{\partial \overline{u}/\partial y} \quad (7)$$

Compressible:

$$Pr_t = \frac{\overline{u'v'}}{\overline{v'h'}} \frac{\partial \overline{T}/\partial y}{\partial \overline{u}/\partial y} \quad (8)$$

Reynolds averaged quantities are used for the incompressible formulation in Eq. 7, whereas Favre averaged values are included in the compressible definition in Eq. 8.

Fig. 4 shows the turbulent Prandtl number at the cold and hot wall over the wall normal distance $y^+ = y/l^+$ with $l^+ = \mu_w/(u_\tau \rho_w)$. A relatively constant turbulent Prandtl number is observed in region II at the hot wall, which is in accordance with ideal gas studies, cf. Kays (1994). This is not surprising, since the compressibility factor (not shown) is close to one and the molecular Prandtl number does not change significantly close to the hot wall ($0.76 < Pr < 0.9$). Approaching the hot wall in region I Pr_t increases up to 1.11 and region III features a linear decrease violating the SRA. For a better prediction of the behavior in region I, a higher resolution at the wall is required. Only a minor difference is observed between the compressible and incompressible formulation and between the two simulations, leading to the conclusion,

that minor compressible effects are present at the hot wall. The turbulent Prandtl number at the cold wall varies strongly close to the pseudo-boiling positions indicated by a purple line. Both formulations feature an s-shaped profile in the vicinity of y_{pb} with different intensities. With increasing bulk pressure in TCF57 and a milder specific heat capacity peak, the difference between the Reynolds and Favre averaged formulations is shrinking and the s-shape is stretched out. In contrast to the hot wall no constant turbulent Prandtl number is observed for both formulations. Hence, the turbulent Prandtl number variation is more intense at the cold wall in the vicinity of y_{pb} and increases as one gets closer to the critical pressure.

So far, we have used common turbulent Prandtl number formulations from the literature, which are applicable for a wide range of flows, but at a closer look both are not suitable for transcritical channel flows. In general, applying a Favre averaging on the governing equations results in the Reynolds stress tensor $\overline{\rho u_i' u_j'}$ for the momentum equations and in the turbulent heat flux $\overline{\rho u_i' h'}$ for the energy equation, where h is the enthalpy. Since transcritical and supercritical fluids are characterized by strong non-linear property variations induced by intermolecular repulsive forces in the vicinity of the PBL, the enthalpy is not proportional to the temperature as for a calorically perfect gas. In Fig. 5 the enthalpy is compared with the relation $c_p T$, which is used for calorically perfect gas. All three quantities are taken from the NIST data base and the profiles are normalized with the value at the hot wall. The profiles are plotted over the scaled temperature range present in the channel at the bulk pressure of $p_b = 47\text{ bar}$. A strong deviation is observable close to the pseudo-boiling position ($0 < \theta_T < 0.25$), where the enthalpy has a change in the slope, but does not show a peak. This peak featured by the perfect gas relation stems from the heat capacity, which can be seen in Fig. 3(d). Since the relation $c_p T$ for a calorically perfect gas leads to a significant error in the vicinity of the pseudo-boiling, we suggest to use an enthalpy based turbulent Prandtl number formulation for transcritical channel flows:

$$Pr_t = \frac{\overline{u'v'}}{\overline{v'h'}} \frac{\partial \overline{h}/\partial y}{\partial \overline{u}/\partial y} \quad (9)$$

Fig. 6 shows the turbulent Prandtl number profiles based on the new formulations at the cold and the hot wall. For comparison, also the compressible formulation using temperature is included. Since the specific heat capacity change is relatively small over the hot wall boundary layer, the enthalpy can be approximated using the relation for a calorically perfect gas $h \approx c_p T$. For this reason, all three profiles coincide and feature a relatively constant value in region II at the hot wall. In Fig. 6 (a), the s-shape disappears in region II using the enthalpy based formulation compared to the compressible definition of Pr_t .

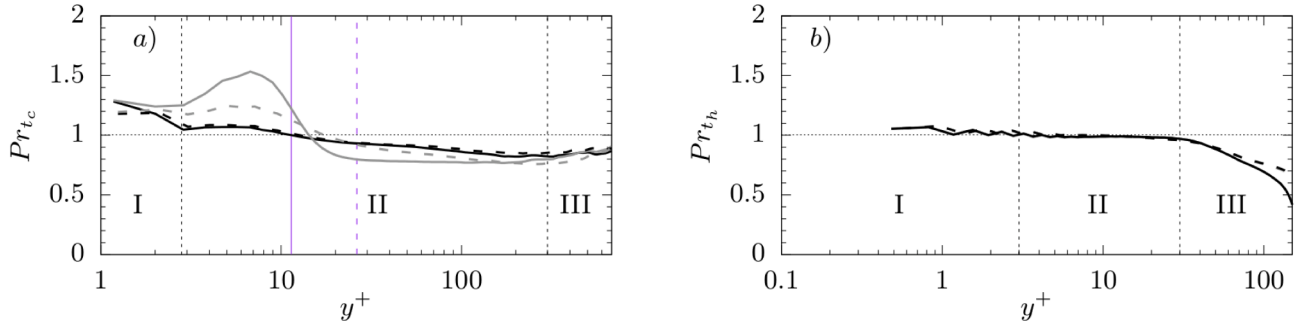


Fig. 6. Turbulent Prandtl number at the cold wall (a) and the hot wall (b) over wall units y^+ for case TCF47 — and TCF57 ----. Included are the compressible (grey) and enthalpy (black) formulation. The pseudo boiling position at the cold wall is indicated by a vertical purple line.

Furthermore, the turbulent Prandtl number increases approaching the cold wall as it is observed at the hot wall. An additional positive effect using the enthalpy formulation is the good agreement between TCF47 and TCF57 for the most part of the boundary layer.

In the following, the influence of pseudo-boiling on the turbulent shear stress and the heat flux is analyzed, since they are included in the turbulent Prandtl number formulation. Based on the work of Huang et al. (1995), both components can be split in three parts

$$\overline{u''v''} = \overline{u'v'} - \overline{u''v''} + \frac{\overline{\rho'u'v'}}{\overline{\rho}}, \quad (10)$$

$$\overline{v''h''} = \overline{v'h'} - \overline{v''h''} + \frac{\overline{\rho'v'h'}}{\overline{\rho}}. \quad (11)$$

His analysis has shown, that the second term in Eqs. 10 and 11 is only 1% of the total and is confined to the sublayer ($y^* < 17$) in compressible channel flows. Thus, the second term can be neglected. For the normalization of the terms the semi-local friction velocity $u_\tau^* = (\tau_w/\rho)$ and enthalpy $h_\tau^* = q_w/(\rho u_\tau^*)$ are used. In order to align the peak positions for the different cases the semi-local wall distance $y^* = y u_\tau^*/\mu$ is applied. Using semi-local values leads to a better collapse between

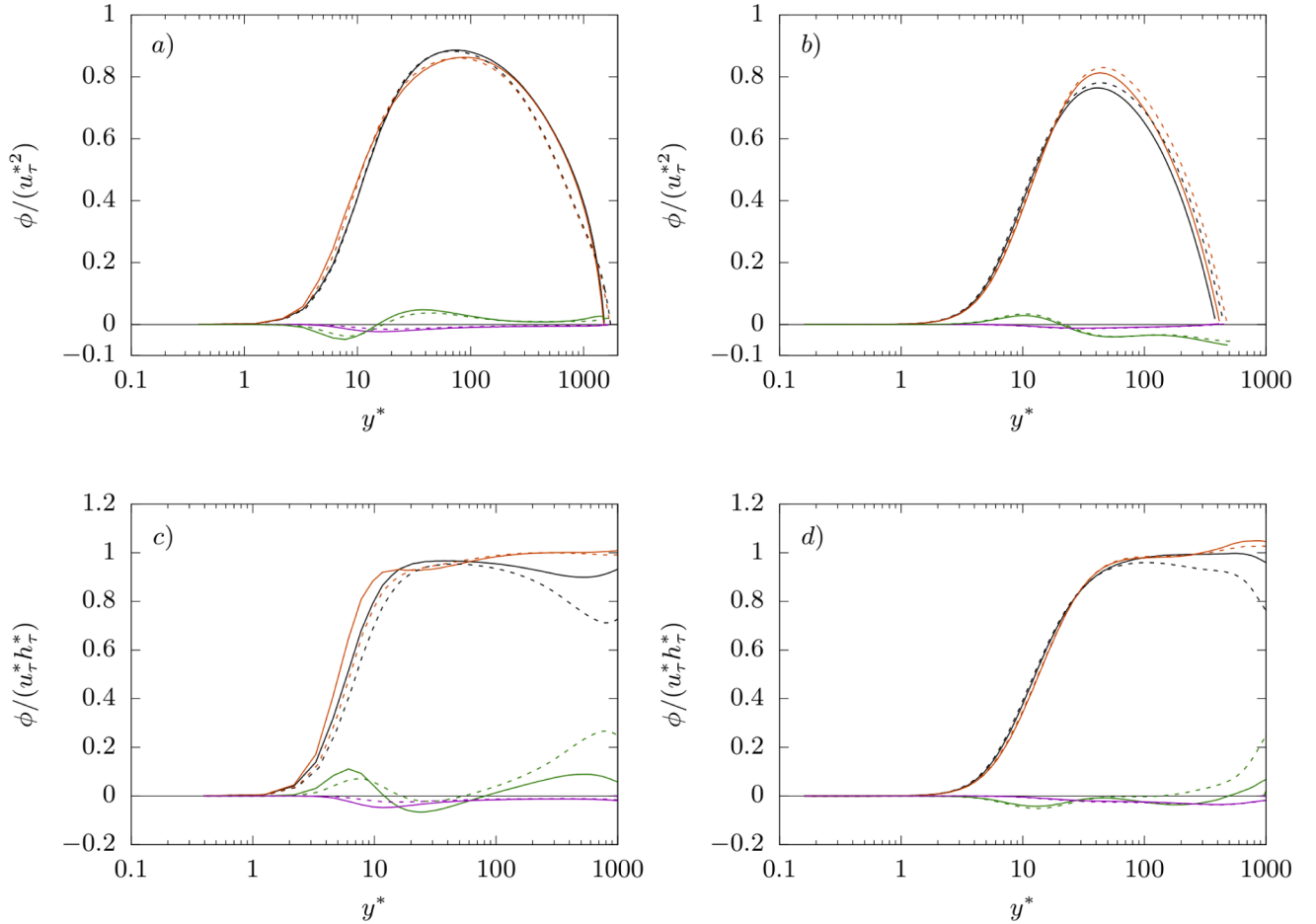


Fig. 7. Terms of Favre averaged turbulent shear stress (a,b) and turbulent heat flux (c,d) normalized with semi-local values over semi-local wall units. The cold wall is shown on the left (a,c) and the hot wall on the right (b,d) with Case TCF47 — and TCF57 ----. Colors: ϕ represents $\overline{u''v''}$ and $\overline{v''h''}$ —; $\overline{u'v'}$ and $\overline{v'h'}$ —; $\overline{\rho'u'v'}$ and $\overline{\rho'v'h'}$ —.

TCF47 and TCF57 compared to a scaling using constant wall properties. The comparison between these two scalings is shown in Appendix B. These observations have also been presented by Patel et al. (2016). The contribution of each term to the total Favre averaged quantity is computed by dividing the respective term by the total Favre averaged stress or flux. Fig. 7(a) and (b) show, that the second and third term of turbulent shear stress are an order of magnitude smaller than the first term. The second term is confined to the buffer and log-layer and reaches 5% and 1.5% of the total shear stress at the cold and hot wall in case TCF47, respectively. It can be observed by comparing to TCF57, that an increase of the property variations leads to slightly higher contributions of the second term. The triple correlation is characterized by an s-shaped profile around zero and contributes to the total shear stress by approximately 25% and 9% at the cold and hot wall in case TCF47, respectively. Hence, the triple correlation has to be taken into account if strong property variations are observed, whereas the second term is negligible, as already observed in compressible flows by Huang et al. (1995). The total shear stress collapses from the wall to the peak position for the two cases, which can also be seen in the study by Patel et al. (2016).

Similar trends can be seen for the turbulent heat flux in Fig. 7(c) and (d). The second term is small enough at both walls in order to be neglected. The triple correlation also features an s-shape with a higher contribution to the total flux compared to the turbulent shear stress. Furthermore, the pseudo-boiling affects the intensity of the second and third term in comparison between the two cases TCF47 and TCF57. The cooling and heating of the walls result in a one-way heat flow towards the cold wall. This leads to an s-shaped temperature profile as shown in Fig. 3 and a heat flux, which does not have a zero crossing. This can be seen in the turbulent heat flux profile, which stays relatively constant throughout the log- and outer layer instead of decreasing after a peak value, as it is the case for the turbulent shear stress.

4.3. Towards RANS modeling

We have shown that the turbulent Prandtl number is not constant in transcritical flows. In order to improve the prediction capabilities of RANS a correct representation of the turbulent stresses and the turbulent Prandtl number is required.

In the following, turbulent Prandtl number models given by Kays and Crawford (1993) and Bae (2016), which are derived using different assumption and models, are assessed. We evaluate these assumptions

with regard to transcritical flows, before comparing their models with the present Pr_t distribution from our LES. At first, a distance l , which is referred to as a 'mixing length', is used to derive the Reynolds analogy for the turbulent heat transfer. Classically, this mixing length is associated with the turbulent viscosity and the turbulent shear stress

$$\widetilde{u''v''} \sim -\epsilon_M \frac{d\bar{u}}{dy} - l^2 \left| \frac{d\bar{u}}{dy} \right| \frac{d\bar{u}}{dy}. \quad (12)$$

In order to determine the turbulent eddy viscosity without the knowledge of the mean velocity distribution Prandtl (1925) assumed, that the size of the eddies is proportional to their distance to the wall leading to $l = \kappa y$, where κ is the von Kármán constant. The following evaluation of the mixing length for transcritical flows is based on Pirozzoli (2014). We use the turbulent eddy viscosity and the velocity gradient for a posteriori analysis.

$$\frac{l_M(\eta)}{H} = \frac{-\sqrt{\widetilde{u''v''}}}{u_\tau} \left(\frac{d\bar{u}}{d\eta} \right)^{-1}, \quad (13)$$

with $\eta = y/H$. Fig. 8(a) and (b) show the Prandtl mixing length hypothesis and a formulation derived from the stress balance

$$\frac{l_M(\eta)}{H} = \kappa\eta \quad (\text{black line}), \quad (14)$$

$$\frac{l_M(\eta)}{H} = \kappa\eta(1-\eta)^{0.5} \quad (\text{pink line}). \quad (15)$$

The log-law region is indicated by vertical lines and determined graphically by observing u^+ over y^+ . It has to be mentioned that the Reynolds number is relatively low and an extensive log-law region does not develop. The mixing length at the cold wall shows for both scaling laws the same behavior of a decrease after a peak value. No plateau can be observed within the indicated log-law region that would indicate a constant value κ . At the heated wall the Prandtl mixing length hypothesis features the same behavior whereas the stress balance formulation has a plateau at $\kappa \approx 0.375$. Pirozzoli (2014) observed in his DNS, that the Prandtl mixing length hypothesis performs worse compared to the stress balance scaling. This is in agreement with our observations at the heated wall, but strong property variations affect the stress balance formulation at the cold wall.

The near wall behavior of the turbulent eddy viscosity and thermal

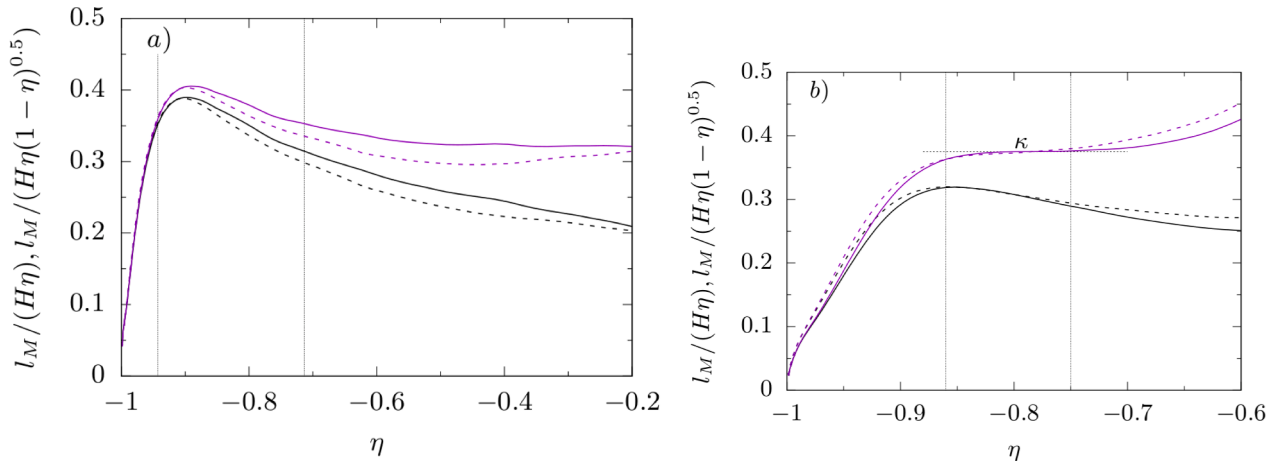


Fig. 8. Mixing length with different scaling at the cold (a) and hot (b) wall over the wall normal distance $\eta = y/H$. The lengths for case TCF47 ——— and TCF57 - - - - are scaled with respect to the wall distance $l_m/(H\eta)$ in black and with respect to the momentum balance $l_m/(H\eta(1-\eta)^{0.5})$ in pink. The beginning and ending of the log-law region are indicated by vertical lines.

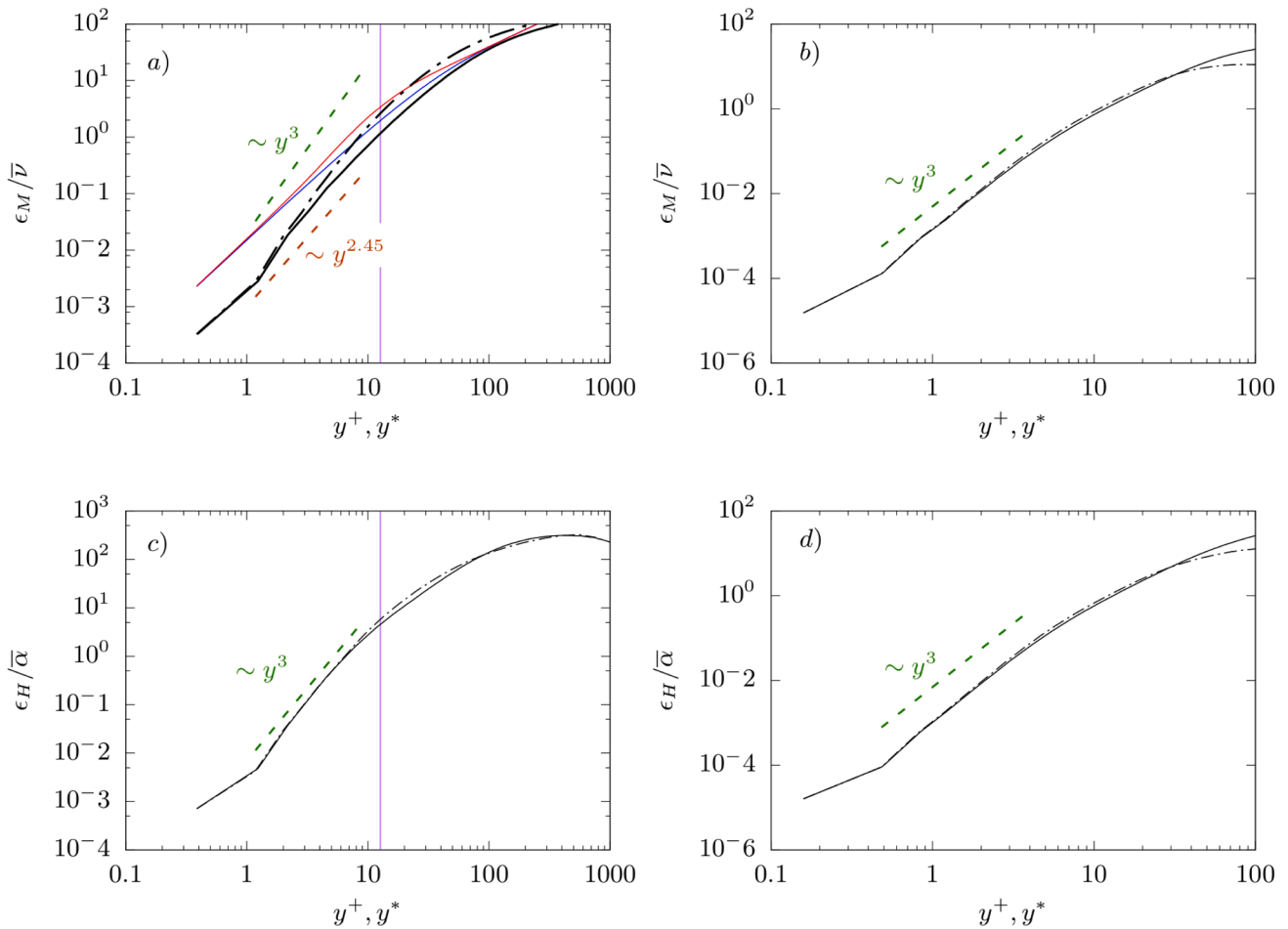


Fig. 9. Turbulent eddy viscosity ϵ_M and eddy thermal diffusivity ϵ_H are scaled with the mean kinematic viscosity $\bar{\nu}$ and thermal diffusivity $\bar{\alpha}$, respectively. Only case TCF47 is shown using a semi-local scaling ($\bar{\nu}, \bar{\alpha}$) ——— and values at the walls ($\bar{\nu}_w, \bar{\alpha}_w$) - - - - over y^+ and y^* , respectively. The cold wall is shown in (a,c) and the hot wall in (b,d). The pink line indicates the pseudo-boiling position for TCF47. The blue line represents $l^+ = \kappa y [1 - \exp(-y^+/A^+)]$ with $A^+ = 26$ and the red line adds the viscosity μ/μ_{w_c} within the damping function.

eddy diffusivity is presented in Fig. 9. It has been shown that both turbulence quantities are proportional to $\sim y^{+3}$ (Kays, 1994; Kim et al., 1987). This proportionality can be derived by Taylor series expansion about y^+ (Antonia and Kim, 1991; Grifoll and Giralt, 2000). In order to see the influence of property variations, we scaled both quantities with the kinematic viscosity $\bar{\nu}$ and thermal diffusivity $\bar{\alpha}$ profiles and with the respective values at the wall. In regard to this scaling y^* and y^+ have

been used, respectively. The profiles of the turbulent eddy viscosity and the thermal eddy diffusivity are only shown for case TCF47, since they are representative for both cases. The comparison between the two scalings shows only minor differences except for the eddy viscosity at the cold wall. Thus, the pseudo-boiling has a higher impact on the eddy viscosity than on the eddy diffusivity, which leads to the linear decrease of the turbulent Prandtl number in region I in Fig. 6(a). In contrast, the

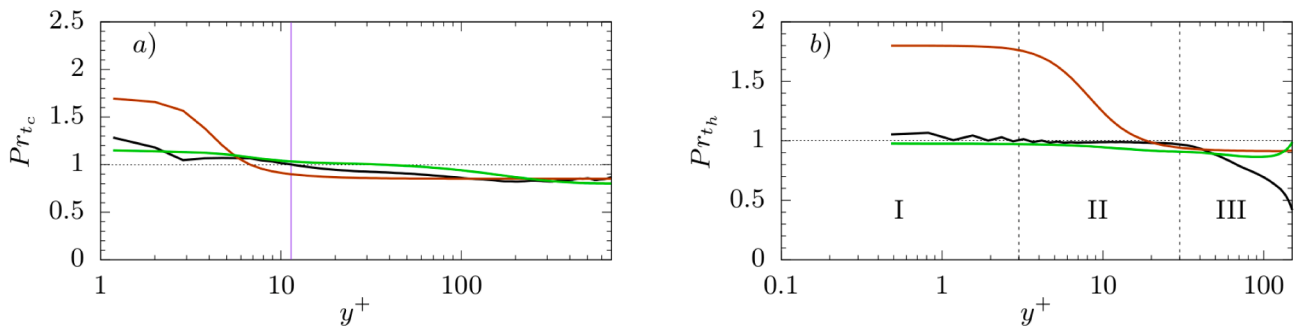


Fig. 10. Turbulent Prandtl number at the cold wall (a) and at the hot wall (b) over wall units y^+ for case TCF47 ———. Included are the turbulent Prandtl number formulation by Kays (1994) ——— and the modified formulation by Bae (2016) ———. The pseudo boiling position at the cold wall is indicated by a vertical purple line.

hot wall features nearly identical profiles for the eddy viscosity and the eddy diffusivity, which result in a constant turbulent Prandtl number distribution in Fig. 6(b).

In order to capture the near wall effects using Prandtl's mixing length hypothesis, van Driest added a damping function

$$l^+ = \kappa y [1 - \exp(-y^+/A^+)]. \quad (16)$$

Griffoll and Giralt (2000) showed that the damping function results in a proportionality with $\tilde{y}^+{}^4$. They modified the van Driest constant A^+ in order to obtain $\tilde{y}^+{}^3$. The new constant does not have the correct dependence on y^+ , but it introduces two additional constants, which have to be adjusted at each wall. Steiner and Irrenfried (2019) included a viscosity ratio within the damping function, which does account for property variations. This leads to an adjustment of the mixing length for $y^+ > 5$ at the cold wall, but still no generally applicable constant A^+ was provided.

After the analysis of the mixing length and near wall behavior of the turbulent eddy viscosity and eddy thermal diffusivity, the enthalpy based turbulent Prandtl number is compared to the formulation by Kays and Crawford (1993) and Bae (2016) in Fig. 10. We modified the original formulation by Bae by replacing $c_p T$ with the enthalpy, which results in a new $Pr_{t,0}$ definition. Furthermore, the damping function was removed, since the turbulent Prandtl number in TCF47 and TCF57 increases towards the wall:

$$Pr_{t,Bae} = C + f_2 Pr_{t,0}, \quad (17)$$

with

$$f_2 = 0.5 \left[1 + \tanh\left(\frac{10 - y^+}{200}\right) \right],$$

and

$$Pr_{t,0} = \frac{1 + \frac{\tilde{u}}{\tilde{\rho}} \left| \left(\frac{\partial \tilde{p}}{\partial y} / \frac{\partial \tilde{u}}{\partial y} \right) \right| + \frac{\tilde{h}}{\tilde{\rho}} \left| \frac{\partial \tilde{p}}{\partial y} \right|}{1 + \frac{\tilde{h}}{\tilde{\rho}} \left| \left(\frac{\partial \tilde{p}}{\partial y} / \frac{\partial \tilde{h}}{\partial y} \right) \right| + \frac{\tilde{u}}{\tilde{\rho}} \left| \frac{\partial \tilde{p}}{\partial y} \right|}$$

The formulation by Kays taken from Eq. (13-7) in Kays and Crawford (1993) is in good agreement at the cold wall for $y^+ > 6$, but in the viscous sublayer it tends to overpredict Pr_t at both walls. The constant C_{Kays} is set to 0.3 and $Pr_{t,\infty}$ to 0.85 at the cold wall and 0.9 at the hot wall. The adjusted Eq. 17 originally by Bae (2016) is in good agreement with Pr_t at both walls after adjusting C to 0.8 at the cold wall and to 0.5 at the hot wall.

5. Conclusion

We investigated a turbulent transcritical channel flow imposing different wall temperatures, thus, enclosing the pseudo-boiling

Appendix A. Validation

We additionally performed LES simulations of a channel flow with a bulk Reynolds number of $Re_b = 2HU_b/\nu = 21950$ and a friction Reynolds number of $Re_\tau = 590$ (Moser et al., 1999) in order to assess the used LES methodology. The Reynolds numbers are in the range of the performed transcritical LES. Three grid levels are investigated in order to show a grid convergence towards the DNS results. Grid parameters and the obtained resolution are presented in Table A.3. The working fluid is air at a bulk pressure of 1 bar and isothermal no-slip walls at 293 K. No gravity or roughness effects are included. Fig. A.11(a) shows the van Driest transformed mean velocity profiles over the wall normal distance y^+ . With increasing grid resolution the velocity profile approaches the DNS result. A good agreement between the LES and the DNS is observed for TCF_2. The Reynolds stresses

temperature using a well-resolved LES. The fully compressible Navier–Stokes equations have been solved and an adaptive look-up table method has been used for thermodynamic and transport properties. The mean velocity distribution is shifted towards the hot wall leading to different boundary layer thicknesses. Strong property variations in the vicinity of the pseudo-boiling position are observed by means of the molecular Prandtl number, which showed a peak value close to the cold wall. The peak correlates with minimum heat diffusivity leading to a flattening of the mean temperature. As a consequence, the resolution requirements are governed by the thermal scales at the cold wall and by the viscous scales at the hot wall. A grid convergence study for transcritical flows is challenging due to the non-linearity of the thermodynamics. The bulk pressure at each grid level varies due to the adjustment of the wall shear stress and the heat flux. Thus, the bulk density has to be adjusted by trial and error to obtain comparable results at each grid level.

The turbulent Prandtl number is relatively constant and does not depend on the turbulent eddy thermal diffusivity definition at the hot wall, which was ascribed to mild changes of thermodynamic properties. Only the enthalpy based turbulent Prandtl number was unaffected by the pseudo-boiling at the cold wall, whereas the temperature based ones show strong variations. The analysis of the three terms, which form the Favre averaged turbulent shear stress and heat flux shows an increased contribution of the triple correlation.

The turbulent Prandtl number models by Kays and Crawford (1993) and Bae (2016) are able to reproduce the LES distribution by adjusting the model parameters, which are different for each wall. Since these models are based on a mixing length, a better knowledge of the momentum and heat exchange in variable molecular Prandtl number flows has to be deduced in order to improve turbulent Prandtl number models, instead of adjusting model parameters, which are not universal.

Declaration of Competing Interest

The authors declare that they have no known competing financial interests or personal relationships that could have appeared to influence the work reported in this paper.

Acknowledgments

The authors gratefully acknowledge the financial support provided by the German Research Foundation (Deutsche Forschungsgemeinschaft-DFG) within the framework of the Sonderforschungsbereich Transregio 40, SFB-TRR40 (Technological foundations for the design of thermally and mechanically highly loaded components of future space transportation systems). Computational resources have been provided by the Leibniz Supercomputing Centre Munich (LRZ). Furthermore, we would like to thank Christian Stemmer for the discussions during the review process.

Table A.3
Summary of grid parameters for TTCF.

	TCF_0	TCF_1	TCF_2
$N_x \times N_y \times N_z$	$48 \times 48 \times 48$	$96 \times 96 \times 96$	$192 \times 192 \times 192$
$L_x \times L_y \times L_z$	$2\pi H \times 2H \times \pi H$	$2\pi H \times 2H \times \pi H$	$2\pi H \times 2H \times \pi H$
Δx^+	65.5	38.2	20.3
Δz^+	32.7	19.1	10.1
$\Delta y^+_{\min} \times \Delta y^+_{\max}$	3.31×43.1	1.85×25.2	0.96×13.4

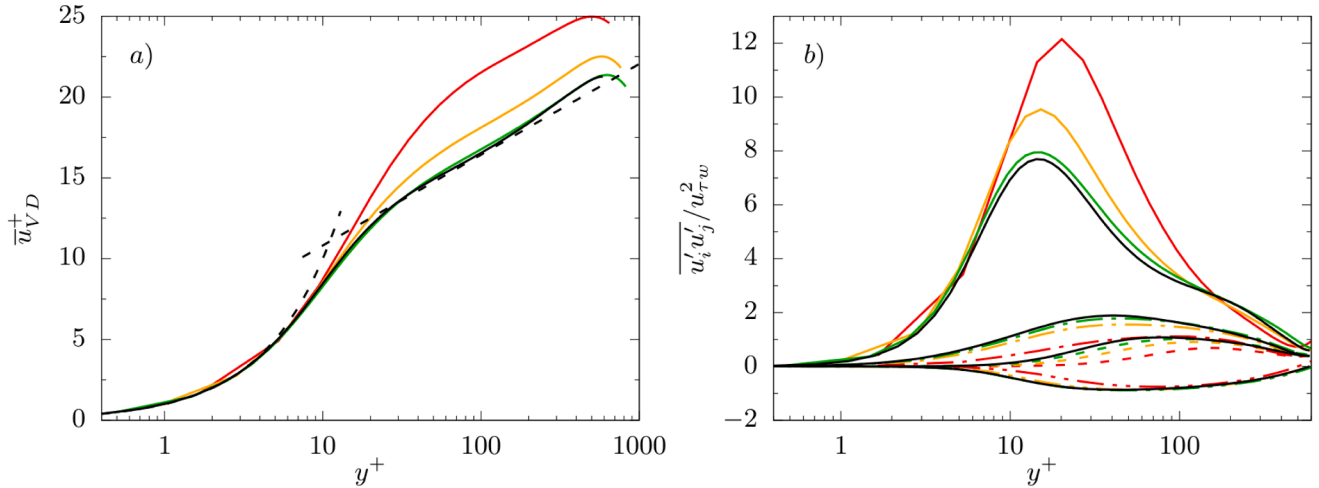


Fig. A.11. Mean velocity profiles using van Driest scaling and Reynolds stresses scaled with the friction velocity are plotted over wall units. The results for the respective grid level are indicated with red for TCF_0, orange for TCF_1 and green for TCF_2 including black for the DNS (Moser et al., 1999). Reynolds stresses $u' u'$ —, $v' v'$ -----, $w' w'$ -.-.-.- and $u' v'$

are presented in Fig. A.11(b) following the same trend as the mean velocity. With increasing grid resolution the peak of the streamwise Reynolds stress $u' u'$ is decreasing and moving towards the wall. A minor overprediction is observed in the buffer and logarithmic layer. The other stresses $v' v'$, $w' w'$ and $u' v'$ converge towards the DNS data with increasing resolution.

Appendix B. Semi-local scaling

In Fig. 7 the Favre average turbulent shear stress and turbulent heat flux from Eqs. 10 and 11 are scaled with semi-local values. The comparison between a scaling using semi-local values and wall properties is presented in Fig. B.12. The advantage of the semi-local scaling is observed especially at the cold where the pseudo-boiling is present. The Favre averaged turbulent shear stress collapses for TCF47 and TCF57 up to $y^* \approx 100$ whereas using wall properties leads to diverse profiles for the two simulations. At the hot wall both scaling laws achieve a good agreement between the two cases. Noticeable is the difference in magnitude obtained by the scaling laws at both wall. Regarding this, the semi-local adjusts the magnitude between both walls.

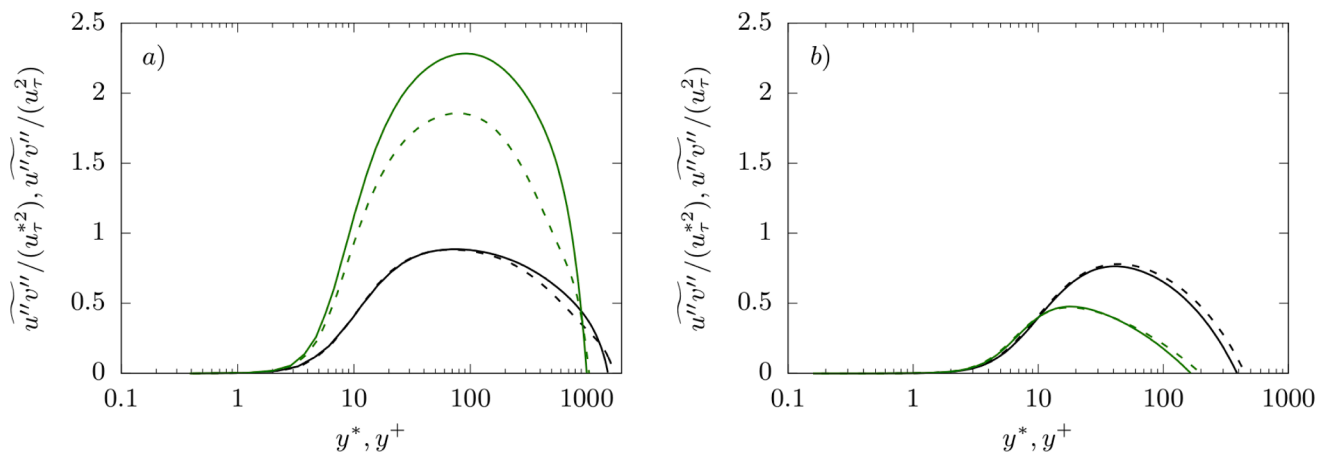


Fig. B.12. Favre averaged turbulent shear stress $\widetilde{u''v''}$ is shown at the cold wall (a) and the hot wall (b). Black lines indicate normalized profiles with semi-local values over semi-local wall units and green lines indicate normalized profiles using wall properties for Case TCF47 — and TCF57 ---- .

Appendix C. Grid sensitivity study

A grid sensitivity study has been performed for case TCF47, since the bulk pressure is closer to the critical point resulting in stronger gradients. The domain extensions have not been changed and the bulk pressure of each level is between 4.75 bar and 4.81 bar. LvL3 is the resolution which has been used in the main text, see Table 1. The main parameters for the considered grids included in the sensitivity study are summarized in Table C.4.

In Fig. C.13 the van Driest transformed velocity profile is shown. It can be observed, that the velocity profile at both walls approaches the analytical logarithmic law. The velocity profile at the hot wall shows no difference between LvL2 and LvL3 indicating a converged solution. In contrast, no converged solution is not observed at the cold wall.

The Reynolds stresses normalized with the semi-local friction velocity are presented in Fig. C.14. At both walls the wall normal and spanwise velocity show minor differences between grid level LvL2 and LvL3 indicating a sufficient resolution for LvL3. For the streamwise direction the peak value is still adjusting for the finest grid level at the cold wall, whereas no difference is observed for the Reynolds stress profile uu at the hot wall.

The near wall temperature profile over the wall normal distance y^+ is depicted in Fig. C.15. A fitted linear function is included in blue and red for the cold and hot wall, respectively. Although, the thermal scales at the cold wall are slightly under-resolved still the temperature profile features a

Table C.4
Summary of grid parameters for the sensitivity study related to case TCF47.

	LvL0	LvL1	LvL2	LvL3
$N_x \times N_y \times N_z$	$48 \times 48 \times 48$	$96 \times 96 \times 96$	$128 \times 128 \times 128$	$192 \times 192 \times 192$
$L_x \times L_y \times L_z$			$2\pi H \times 2H \times \pi H$	
$\Delta x_{\text{cold}}^+ \times \Delta x_{\text{hot}}^+$	69×31	39×18	32×14	23×10
$\Delta z_{\text{cold}}^+ \times \Delta z_{\text{hot}}^+$	35×16	20×9	16×7	12×5
$\Delta y_{\text{min,cold}}^+ \times \Delta y_{\text{min,hot}}^+$	2.50×1.11	1.35×0.62	1.09×0.48	0.77×0.32
$\Delta y_{\text{max,cold}}^+ \times \Delta y_{\text{max,hot}}^+$	50.0×22.5	28.4×13.1	23.2×10.2	16.8×6.9

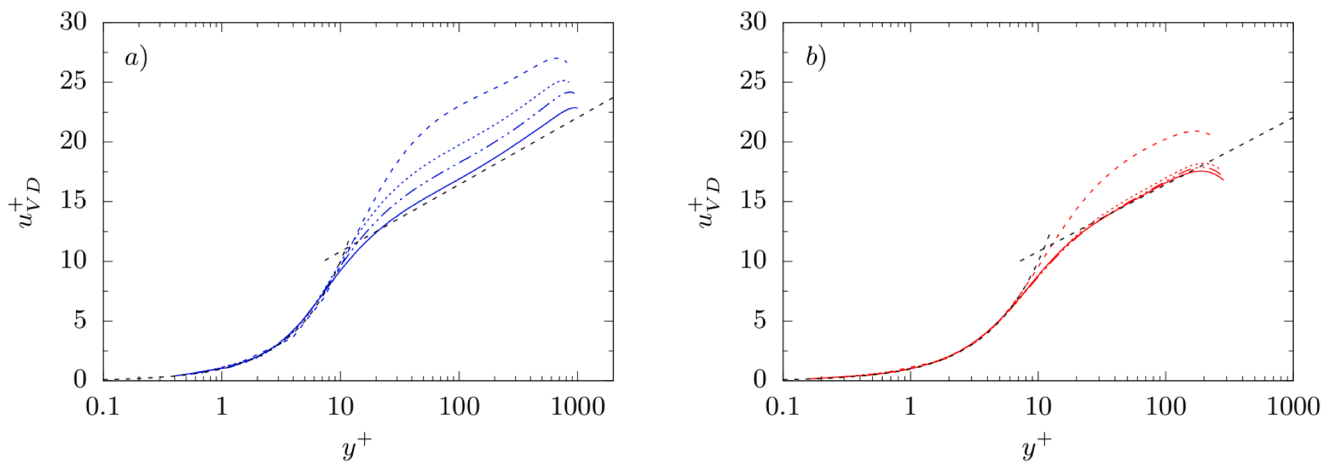


Fig. C.13. Van Driest normalized velocity profiles for case TCF47 at different grid levels: LvL0 ---, LvL1 ·····, LvL2 - · - ·, LvL3 ———. The viscous sublayer and the logarithmic law are indicated with black dashed lines based on the constants $B = 5.2$ and $\kappa = 0.41$. The cold and hot wall are presented in subfigure a) and b), respectively.

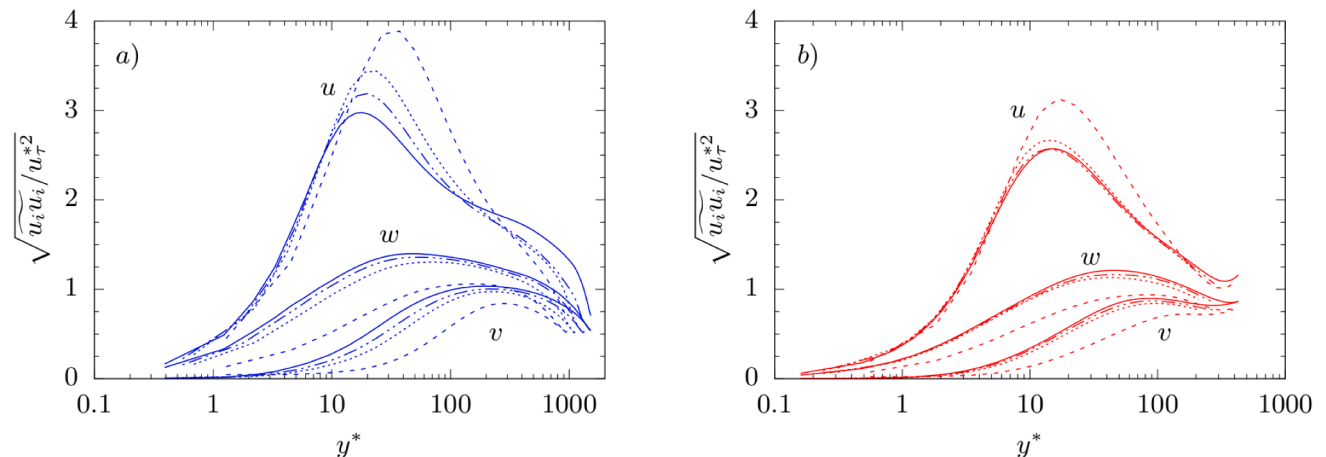


Fig. C.14. Reynolds stresses normalized with the semi-local friction velocity $u^* = \sqrt{\tau_w/\rho}$ for case TCF47 at different grid levels: LvL0 ---, LvL1 ·····, LvL2 - · - ·, LvL3 ———. The cold and hot wall are presented in subfigure a) and b), respectively.

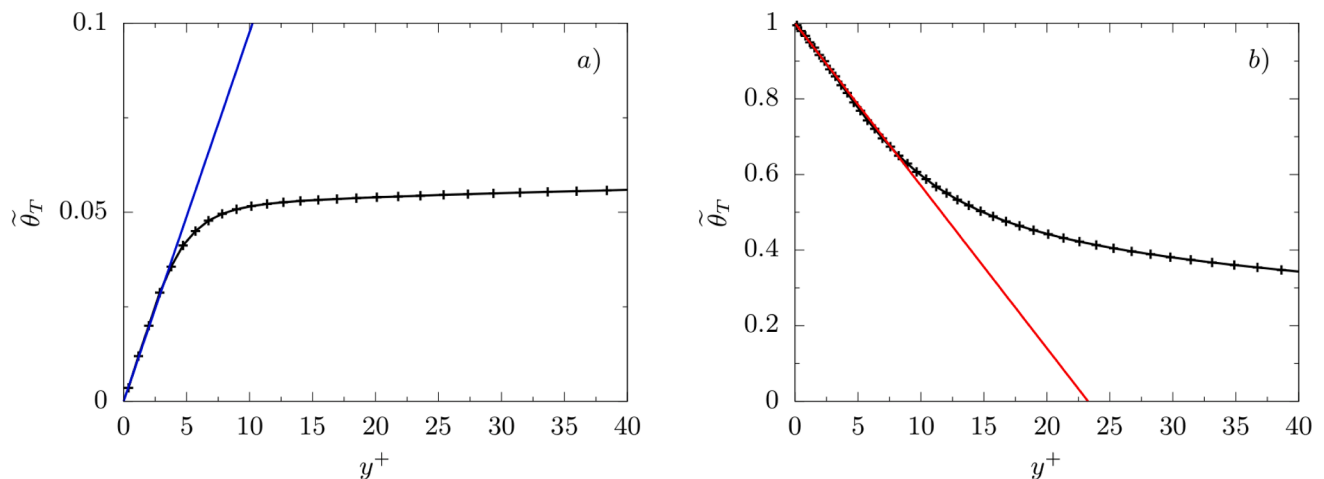


Fig. C.15. Scaled temperature profile $\tilde{\theta}_T$ at the cold wall (a) and hot wall (b) over the scaled wall normal distance y^+ . The blue and red line indicate a fitted linear function. The symbols in the temperature profile correspond to the cell center values.

linear distribution at the walls (viscous sublayer). From this, we conclude that the proposed ratio in Eq. 3 provides a reasonable estimation of the thermal scales.

References

- Antonia, R.A., Kim, J., 1991. Turbulent Prandtl number in the near-wall region of a turbulent channel flow. *International Journal of Heat and Mass Transfer* 34, 1905–1908.
- Bae, Y.Y., 2016. A new formulation of variable turbulent Prandtl number for heat transfer to supercritical fluids. *International Journal of Heat and Mass Transfer* 92, 792–806.
- Brun, C., Boiarciuc, M.P., Haberkorn, M., Comte, P., 2008. Large eddy simulation of compressible channel flow. *Theoretical and Computational Fluid Dynamics* 22, 189–212.
- Doehring, A., Schmidt, S.J., Adams, N.A., 2018. Numerical Investigation of Transcritical Turbulent Channel Flow, in: 2018 Joint Propulsion Conference.
- Egerer, C.P., Schmidt, S.J., Hickel, S., Adams, N.A., 2016. Efficient implicit LES method for the simulation of turbulent cavitating flows. *Journal of Computational Physics* 316, 453–469.
- Grifoll, J., Giralt, F., 2000. The near wall mixing length formulation revisited. *International Journal of Heat and Mass Transfer* 43, 3743–3746.
- Hickel, S., Adams, N.A., Domaradzki, J.A., 2006. An adaptive local deconvolution method for implicit LES. *Journal of Computational Physics* 213, 413–436.
- Hickel, S., Egerer, C.P., Larsson, J., 2014. Subgrid-scale modeling for implicit large eddy simulation of compressible flows and shock-turbulence interaction. *Physics of Fluids* 26.
- Huang, P.G., Coleman, G.N., Bradshaw, P., 1995. Compressible turbulent channel flows: DNS results and modelling. *Journal of Fluid Mechanics* 305, 185–218.
- Kaller, T., Pasquariello, V., Hickel, S., Adams, N.A., 2019. Turbulent flow through a high aspect ratio cooling duct with asymmetric wall heating. *Journal of Fluid Mechanics* 860, 258–299.
- Kawai, S., 2019. Heated transcritical and unheated non-transcritical turbulent boundary layers at supercritical pressures. *Journal of Fluid Mechanics* 865, 563–601.
- Kays, W.M., 1994. Turbulent Prandtl Number-Where Are We? *Journal of Heat Transfer* 116, 284–295.
- Kays, W.M., Crawford, M.E., 1993. *Convective Heat and Mass Transfer*, 3rd ed. McGraw-Hill Inc.
- Kim, J., Moin, P., Moser, R., 1987. Turbulence statistics in fully developed channel flow at low Reynolds number. *Journal of Fluid Mechanics* 177, 133–166.
- Kim, K., Hickey, J.P., Scalo, C., 2019. Pseudophase change effects in turbulent channel flow under transcritical temperature conditions. *Journal of Fluid Mechanics* 871, 52–91.
- Lee, J., Jung, S.Y., Sung, H.J., Zaki, T.A., 2013. Effect of wall heating on turbulent boundary layers with temperature-dependent viscosity. *Journal of Fluid Mechanics* 726, 196–225.
- Lemmon, E.W., Huber, M.L., McLinden, M.O., 2013. NIST Standard Reference Database 23: Reference Fluid Thermodynamic and Transport Properties-REFPROP, Version 9.1. National Institute of Standards and Technology.
- Ma, P.C., Yang, X.I.A., Ihme, M., 2018. Structure of wall-bounded flows at transcritical conditions. *Physical Review Fluids* 3 (3).
- Matheis, J., Hickel, S., 2018. Multi-component vapor-liquid equilibrium model for LES of high-pressure fuel injection and application to ECN Spray A. *International Journal of Multiphase Flow* 99, 294–311.
- Mayer, W., Tamura, H., 1996. Propellant Injection in a Liquid Oxygen/Gaseous Hydrogen Rocket Engine. *Journal of Propulsion and Power* 12, 1137–1147.
- Monin, A.S., Yaglom, A.M., 1975. *Statistical Fluid Mechanics: Mechanics of Turbulence*, vol. 2. MIT Press.
- Moser, R.D., Kim, J., Mansour, N.N., 1999. Direct numerical simulation of turbulent channel flow up to $Re_\tau = 590$. *Physics of Fluids* 11, 943–945.
- Patel, A., Boersma, B.J., Pecnik, R., 2016. The influence of near-wall density and viscosity gradients on turbulence in channel flows. *Journal of Fluid Mechanics* 809, 793–820.
- Pirozzoli, S., 2014. Revisiting the mixing-length hypothesis in the outer part of turbulent wall layers: mean flow and wall friction. *Journal of Fluid Mechanics* 745, 378–397.
- Prandtl, L., 1925. 7. Bericht über Untersuchungen zur ausgebildeten Turbulenz. *ZAMM - Journal of Applied Mathematics and Mechanics/Zeitschrift für Angewandte Mathematik und Mechanik* 5, 136–139.
- Schmidt, S.J., Sezal, I.H., Schnerr, G.H., 2006. Compressible simulation of high-speed hydrodynamics with phase change. In: *European Conference on Computational Fluid Dynamics*.
- Simeoni, G.G., Bryk, T., Gorelli, F.A., Krisch, M., Ruocco, G., M., S., T., S., 2010. The Widom line as the crossover between liquid-like and gas-like behaviour in supercritical fluids. *Nature Physics* 6, 503–507.
- Smits, A.J., Dussauge, J.P., 2006. *Turbulent Shear Layers in Supersonic Flow*, 2nd ed. Springer Science & Business Media Inc.
- Steiner, H., Irrenfried, C., 2019. Modelling of thermal wall boundary conditions with temperature-dependent material properties for use in RANS. *International Journal of Heat and Fluid Flow* 80, 108495.
- Trettel, A., Larsson, J., 2016. Mean velocity scaling for compressible wall turbulence with heat transfer. *Physics of Fluids* 28, 026102.
- Yoo, J.Y., 2013. The Turbulent Flows of Supercritical Fluids with Heat Transfer. *Annual Review of Fluid Mechanics* 45, 495–525.
- Zonta, F., Marchioli, C., Soldati, A., 2012. Modulation of turbulence in forced convection by temperature-dependent viscosity. *Journal of Fluid Mechanics* 697, 150–174.